Excitons and their Fine Structure in Lead Halide Perovskite Nanocrystals from Atomistic GW/BSE Calculations

Giulia Biffi,[†,‡,‖] Yeongsu Cho,[¶,‖] Roman Krahne,[†] and Timothy C. Berkelbach[*,¶,§]

†*Istituto Italiano di Tecnologia, Via Morego 30, 16163 Genova, Italy*
‡*Dipartimento di Chimica e Chimica Industriale, Università degli Studi di Genova, Via Dodecaneso, 31, 16146 Genova, Italy*
¶*Department of Chemistry, Columbia University, New York, New York 10027 USA*
§*Center for Computational Quantum Physics, Flatiron Institute, New York, New York 10010 USA*
‖*These authors contributed equally*

E-mail: t.berkelbach@columbia.edu

Abstract

Atomistically detailed computational studies of nanocrystals, such as those derived from the promising lead-halide perovskites, are challenging due to the large number of atoms and lack of symmetries to exploit. Here, focusing on methylammonium lead iodide nanocrystals, we combine a real-space tight binding model with the GW approximation to the self-energy and obtain exciton wavefunctions and absorption spectra via solutions of the associated Bethe-Salpeter equation. We find that the size dependence of carrier confinement, dielectric contrast, electron-hole exchange, and exciton binding energies has a strong impact on the lowest excitation energy, which can be tuned by almost 1 eV over the diameter range of 2–6 nm. Our calculated excitation energies are about 0.2 eV higher than experimentally measured photoluminescence, and they display the same qualitative size dependence. Focusing on the fine structure of the band-edge excitons, we find that the lowest-lying exciton is spectroscopically dark and about 20–30 meV lower in energy than the higher-lying triplet of bright states, whose degeneracy is slightly broken by crystal field effects.

Introduction

Lead-halide perovskite nanocrystals (LHP NCs), with formula $APbX_3$ where A is a monovalent cation and X is a halide anion, exhibit remarkable electronic and optical properties,[1–3] suggesting promising applications in optoelectronics,[4–8] photonics,[9,10] and spintronics.[11] Compared to bulk LHPs, LHP NCs display anomalously short radiative lifetimes and concomitant high photoluminescence quantum yields, the origin of which is still under debate.[1–3,12] These interesting optical properties and their temperature dependence have focused attention on the exciton fine structure, i.e., the energy ordering and character of the band-edge excitons.[13?–19] For example, the lowest-energy exciton of Cs-LHP NCs has been suggested to be a bright (emissive) state with total angular momentum $J = 1$, which could explain the high photoluminescence quantum yield.[14–16] This property would be in stark contrast with the case of conventional organic and inorganic semiconductors, where the lowest-energy exciton is a dark (non-emissive) state. Other works have suggested that this conventional behavior persists in the LHP NCs (i.e., the lowest-energy exciton is a dark state with total angular momentum $J = 0$) but that exciton relaxation by phonons is suppressed at low temperatures, yielding long lifetimes for the bright exciton in both NCs[17–19] and 2D LHPs.[?]

The properties of the band-edge excitons—whose energy separations are very small, of the order of 1–10 meV—are influenced by quantum confinement, electron-hole attraction and exchange,[14–16,20] dielectric environment,[21] and lattice structure (including the bulk and surface Rashba effects),[22–25] making precise theoretical predictions an incredible challenge. This complexity has led to the development of exciton models based on effective-mass or $\boldsymbol{k} \cdot \boldsymbol{p}$ Hamiltonians, pioneered especially by Efros and coworkers,[14–16] among others.[20,26] Atomistic simulation, although desirable, is frustrated by the sizes of even the smallest experimentally accessible NCs, which can have hundreds or thousands of atoms. Although atomistic force-fields or density functional theory can be applied to study the ground-state and structural properties of systems of this size,[27–30] accurate excited-state theories are more expensive and generally inaccessible in a fully *ab initio* setting.

Here, we overcome this challenge and construct an atomistic orbital-dependent tight-binding model parametrized by first-principles density functional theory (DFT) calculations, after which we use a model dielectric function to apply self-energy corrections via the GW approximation[31–33] and calculate the energies and properties of excitons via the Bethe-Salpeter equation.[34–36] The computational approach is similar to previous work by two of us on the properties of layered quasi-two-dimensional LHPs.[37] As a specific example, we study methylammonium lead iodide ($MAPbI_3$) NCs, calculating the exciton binding energies, absorption spectra, and band-edge fine structure. Within the approximations of our approach, we find that the lowest-energy exciton is always a dark state.

We study $MAPbI_3$ for several reasons, although our approach is general and could be applied to any LHP NC. First, this LHP is one of the most studied in its bulk form, especially for photovoltaics, partly due to its strong absorption at low energies that facilitates sensitization.[38,39] Moreover, bulk $MAPbI_3$ crystals have low lasing thresholds[40] and are generally more stable than Cs-based ones.[41] For these reasons, the atomic and electronic structure of bulk $MAPbI_3$ has been extensively studied using DFT[42,43] and the GW approximation,[44–47] providing important points of comparison. These valuable properties have motivated experimental studies of $MAPbX_3$ NCs with high photoluminescence quantum yields and controllable size, leading to tunable band gaps. Such $MAPbX_3$ NCs have been realized by colloidal synthesis[48–53] and templated growth inside porous oxide films,[54,55] providing experimental results to which we can directly compare.

Computational Methods

The parameters of our orbital-dependent tight-binding model are determined from a DFT calculation of bulk $MAPbI_3$, which first requires the determination of the crystal structure. (To our knowledge, the crystal structure of LHP NCs is still poorly understood, but the crystal structure of $MAPbI_3$ NCs is likely tetragonal.[1] However, this assumption may be incorrect due to surface effects and/or metastability.) From experiments, it is known that the bulk $MAPbI_3$ exists in an orthorhombic phase below about 160 K, a tetragonal phase between 160 K and 330 K, and a cubic phase above 330 K.[56] The computational prediction of crystal structures in finite temperature phases is nontrivial because of anharmonic effects. In Ref. 43, it was shown that using zero-temperature DFT for the geometry optimization of the tetragonal and cubic phases yields a large inversion symmetry breaking via distortion of the PbI framework, leading to a large bulk Rashba effect. However, these crystal structures disagree with second harmonic generation rotational anisotropy experiments. Therefore, with interest in room-temperature behavior, we reuse the structure proposed in Ref. 43, which was generated by fixing the PbI framework of the tetragonal phase and relaxing only the MA cations, whose orientations yield a small but nonzero Rashba effect. This crystal structure is shown in Fig. 1(a).

With our MA-relaxed crystal structure of bulk $MAPbI_3$, we perform a DFT calculation including spin-orbit coupling, using Quantum Espresso[57] with the PBE exchange-correlation functional,[58] relativistic PAW pseudopotentials, a kinetic energy cutoff of 60 Ry, and a $6 \times 6 \times 6$ k-point mesh. Using wannier90,[59] the DFT solution is used to construct maximally localized Wannier functions (MLWFs) $\phi_\mu(\boldsymbol{r})$, corresponding to I 5s and 5p orbitals and Pb 6s and 6p orbitals, as well as their tight-binding Hamiltonian matrix elements $h_{\mu\nu}$ and dipole matrix elements $r^e_{\mu\nu}$, $e \in \{x, y, z\}$. Greek indices $\mu, \nu, \kappa, \lambda$ will be used throughout to indicate MLWF atomic orbitals, including spin. These real-space tight-binding parameters are then used to build a mean-field Hamiltonian $\mathbf{h}^{\mathrm{NC}}$ of the aperiodic NCs. Our NC surfaces are terminated with halide atoms, in agreement with experimental observations,[49] with exposed facets that are qualitatively equivalent to the (100) surface of a cubic perovskite. We use the same tight-binding parameters for all atoms, even those near the surface of the NCs, which can be understood as an approximate passivation that does not require microscopic specification. However, the details of surface passivation are important for controlling trap states and associated non-radiative recombination.[28,51,53] Similarly, relaxation of the atoms at the surface, which we neglect here, would modify these matrix elements and the resulting electronic structure.[25,28]

With this tight-binding Hamiltonian matrix in the basis of MWLFs $\phi_\mu(\boldsymbol{r})$, we calculate the molecular orbitals $C_{\mu p}$ and orbital energies ε_p, $\mathbf{h}^{\mathrm{NC}}\mathbf{C} = \mathbf{C}\boldsymbol{\varepsilon}$. To the orbital energies, we add two self-energy corrections in the spirit of the many-body GW approximation (at the level of approximation made throughout this work, we do not distinguish degrees of self-consistency in the self-energy, but our calculations are all performed in the one-shot G_0W_0 approximation as described here). The first correction is a rigid shift of the conduction and valence band energies by $\pm\Delta/2$ to correct the bulk band gap to the previously calculated value of 1.67 eV.[44] Our DFT and GW band structures of bulk tetragonal $MAPbI_3$ are shown in Fig. 1, which can be seen to contain a small but nonzero Rashba splitting at the band edges. As is well-known,[44–47] the GW correction to the band gap of LHPs is sizable—about 1.5 eV in our case. Our second self-energy correction within the GW approximation uses a model dielectric function and a static screening approximation to account for dielectric constrast at the NC interface,[60,61] in the style of a GδW calculation.[62] Combining these two corrections, we calculate the GW quasiparticle energies of all conduction (c)

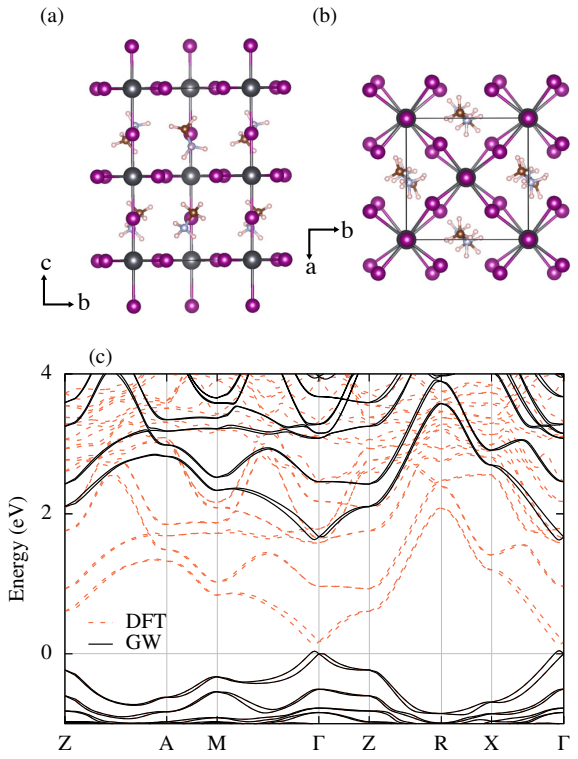

Figure 1: (a,b) Crystal structure of bulk tetragonal $MAPbI_3$ from Ref. 43 and (c) band structure calculated with DFT (PBE with spin-orbit coupling) and rigidly shifted to match the GW band gap.[44]

and valence (v) bands,

$$E_c = \varepsilon_c + \Delta/2 + \sum_\mu |C_{\mu c}|^2 \delta\Sigma(\boldsymbol{r}_\mu) \tag{1a}$$

$$E_v = \varepsilon_v - \Delta/2 - \sum_\mu |C_{\mu v}|^2 \delta\Sigma(\boldsymbol{r}_\mu) \tag{1b}$$

where $\boldsymbol{r}_\mu$ is the position of the atom to which the MLWF $\phi_\mu(\boldsymbol{r})$ belongs,

$$\delta\Sigma(\boldsymbol{r}_1) = \frac{1}{2} \lim_{\boldsymbol{r}_2 \to \boldsymbol{r}_1} \left[W(\boldsymbol{r}_1, \boldsymbol{r}_2) - \frac{1}{\epsilon_{\mathrm{p}} |\boldsymbol{r}_1 - \boldsymbol{r}_2|} \right], \tag{2}$$

and $W(\boldsymbol{r}_1, \boldsymbol{r}_2)$ is the classical Coulomb interaction energy between two charges in the NC at $\boldsymbol{r}_1, \boldsymbol{r}_2$.[60] We use the analytical Coulomb energy of charges in a dielectric cuboid with side lengths L_x, L_y, L_z,[63]

$$W(\boldsymbol{r}_1, \boldsymbol{r}_2) = \sum_{i,j,k=-\infty}^{\infty} \frac{[(\epsilon_{\mathrm{p}} - \epsilon_{\mathrm{env}})/(\epsilon_{\mathrm{p}} + \epsilon_{\mathrm{env}})]^{|i|+|j|+|k|}}{\epsilon_{\mathrm{p}} |\boldsymbol{r}_1 - \boldsymbol{r}_2^{ijk}|} \tag{3a}$$

$$\boldsymbol{r}_2^{ijk} \equiv [(-1)^i x_2 + iL_x, (-1)^j y_2 + jL_y, (-1)^k z_2 + kL_z]. \tag{3b}$$

With the surface termination described above, For a NC made of n^3 octahedra, we use $L_x = L_y = n \times (6.4\ \text{Å}) + 2 \times (1.5\ \text{Å})$ and $L_z = n \times (6.5\ \text{Å}) + 2 \times (1.5\ \text{Å})$, where 6.4 Å and 6.5 Å correspond to the diagonals of the tetragonal octahedra and we have added an additional dielectric buffer region of 1.5 Å on all sides. Throughout this work, we use the bulk $MAPbI_3$ perovskite high-frequency dielectric constant $\epsilon_{\mathrm{p}} = 6.1$ and an environmental dielectric constant of $\epsilon_{\mathrm{env}} = 2.1$, representative of a generic low-dielectric environment, such as organic ligands.[2,8,64] (For large NCs with small exciton binding energies that are on the order of optical phonon fre-

quencies, phonon screening suggests a larger value of ϵ_p or explicit treatment of electron-phonon interactions.[65])

To evaluate the optical and excitonic properties, we calculate the exciton wavefunction as a solution to the Bethe-Salpeter equation (BSE) in the Tamm-Dancoff approximation,

$$|\Psi^N\rangle = \sum_{cv} A^N_{cv} \hat{a}^\dagger_c \hat{a}_v |0\rangle \tag{4a}$$

$$E_N A^N_{cv} = (E_c - E_v) A^N_{cv} + \sum_{c'v'} \left[(cv|V|v'c') - (cc'|W|v'v)\right] A^N_{c'v'}, \tag{4b}$$

where V and W indicate the bare and screened Coulomb interactions and we use (11|22) notation for two-electron integrals. For all results in the next section, we included 200 valence bands and 200 conduction bands in the BSE calculation. In approximate theories of Wannier-type excitons, the exchange interaction is commonly neglected on the basis of its short range, but as it is critical in the determination of the exciton fine structure,[20] we include it here. The bare exchange integral is approximated as

$$(cv|V|v'c') = \sum_{\mu\kappa} C^*_{\mu c} C_{\mu v} C^*_{\kappa v'} C_{\kappa c'} V_{\mu\kappa} + \sum_{\mu\neq\kappa}^{\text{intra}} C^*_{\mu c} C_{\kappa v} C^*_{\kappa v'} C_{\mu c'} (\mu\kappa|\kappa\mu) \tag{5}$$

where $V_{\mu\kappa} = |\boldsymbol{r}_\mu - \boldsymbol{r}_\kappa|^{-1}$ if μ and κ are not on the same atom and $V_{\mu\kappa} = (\mu\mu|\kappa\kappa)$ otherwise. Note that our treatment includes both short-range and long-range exchange effects. The screened Coulomb interaction is approximated similarly but without intra-atomic exchange integrals,

$$(cc'|W|v'v) = \sum_{\mu\kappa} C^*_{\mu c} C_{\mu c'} C^*_{\kappa v'} C_{\kappa v} W_{\mu\kappa} \tag{6}$$

where $W_{\mu\kappa} = W(\boldsymbol{r}_\mu, \boldsymbol{r}_\kappa)$ if μ and κ are not on the same atom and $W_{\mu\kappa} = (\mu\mu|\kappa\kappa)$ otherwise (i.e., the Coulomb interaction is unscreened at the intra-atomic length scale). The intra-atomic repulsion integrals $(\mu\mu|\kappa\kappa)$ and $(\mu\kappa|\kappa\mu)$ for Pb and I s and p orbitals are calculated using PySCF[66,67] with the def2-TZVP basis set.[68]

From the BSE exciton eigenvectors A^N_{cv}, we calculate the polarized absorption spectrum and its average

$$I_e(\omega) \propto \sum_N \left| \sum_{cv} r^e_{cv} A^N_{cv} \right|^2 \delta(\hbar\omega - E_N) \tag{7a}$$

$$I(\omega) = \sum_{e\in\{x,y,z\}} I_e(\omega). \tag{7b}$$

Because of our nonperturbative inclusion of spin-orbit coupling, the molecular orbitals have mixed spin character, i.e., m_s is not a good quantum number. Therefore, the total spin S is not a good quantum number for the exciton wavefunctions and they cannot be separated into spin singlets ($S = 0$) and triplets ($S = 1$) with familiar dipole selection rules. Rather, the spectral intensity of the excited states is determined by the lattice symmetry in combination with the spin and orbital character of the molecular orbitals participating in the dominant transitions. This feature is one of the primary origins of the complex fine structure of low-lying excitons in lead-halide perovskites.

Results and Discussion

We have performed calculations on halide-terminated, cube-shaped NCs containing n^3 octahedra, with n = 3–10, corresponding to a NC edge length $L \approx$ 1.9–6.2 nm; our largest NCs include almost 4300 Pb and I atoms. Assuming a bulk exciton reduced mass of about $\mu = 0.1$[47,69–71] and dielectric constant $\epsilon_p = 6.1$, a hydrogenic calculation predicts a bulk exciton binding energy of $E_b = \mu/\epsilon_p^2 \times (13.6\text{ eV}) = 37$ meV and a Bohr radius of $a_b = \epsilon_p/\mu \times (0.053\text{ nm}) = 3.2$ nm, suggesting that the NCs that we study are in the strong to moderate confinement limits. (This estimated exciton binding energy is 2–3 times larger than the most recent experimental measurements;[69,71]? see discussion in Conclusions.)

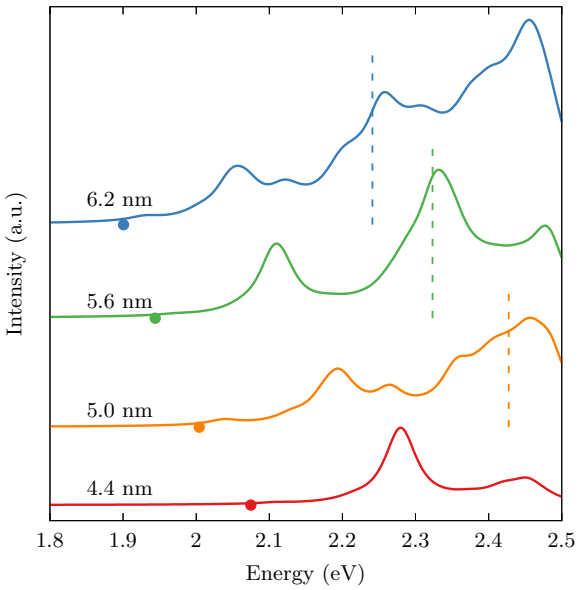

Figure 2: Absorption spectra of $MAPbI_3$ nanocrystals with side length L = 4.4–6.2 nm (n = 7 − 10). The first excitation, always spectroscopically dark, is indicated by a filled circle, while the band gap is indicated by vertical dashed line.

Calculated absorption spectra are shown in Fig. 2, averaged over x, y, and z polarizations. With increasing size, the spectra become more structured and the absorption onset energy is reduced due to the quantum confinement effect. The first excitation energy is indicated by a filled circle and corresponds to a state that is spectroscopically dark (see further discussion below), in agreement with previous studies on $CsPbBr_3$ NCs.[17–19,52] The GW band gap is indicated by vertical dashed lines. For small NCs, the exciton binding energy is large, about 1 eV for L = 2.5 nm (n = 4). For the largest NCs we study, the exciton binding energy drops to about 0.3 eV for L = 6.2 nm (n = 10).

We now investigate the character of the lowest-lying excitons and the associated fine structure. We first review the basic picture of exciton fine structure in LHPs.[14–16,72] The valence band is primarily composed of Pb 6s and I 5p atomic orbitals (with overall s-like symmetry) and is doubly degenerate with $m_s = \pm 1/2$. The conduction band is strongly split by spin-orbit coupling, and the low-energy band is primarily composed of Pb $6p_{j=1/2}$ atomic orbitals and is doubly degenerate with $m_j = \pm 1/2$. This minimal picture suggests three triplet excitons with $J = 1$ and one singlet exciton with $J = 0$, all approximately corresponding to an intra-atomic Pb 6s→6p transition. Basic spectroscopic selection rules suggest that the singlet is dark and the triplet is bright. Excitons arising from the higher-energy conduction band with Pb $6p_{j=3/2}$ character are at least 1 eV higher in energy, due to the large spin-orbit coupling.

For a cubic crystal structure, the bright triplet manifold is degenerate and is higher in energy than the dark singlet exciton $|D\rangle$ due to the electron-hole exchange interaction. For a tetragonal crystal structure, which we use here, the bright triplet degeneracy is broken into a doublet of excitons $|X\rangle, |Y\rangle$ with polarized absorption along x and y and a singlet exciton $|Z\rangle$ with polarized absorption along z, and their energetic order depends on the crystal field splitting. Note

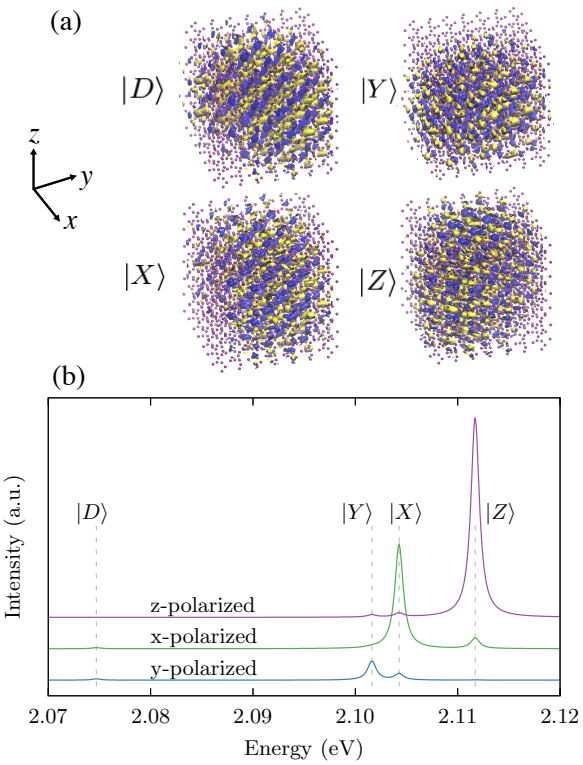

Figure 3: (a) Exciton wavefunction (blue is positive and yellow is negative) of the first four excited states of a $L = 4.4$ nm ($n = 7$) nanocrystal. The axes are defined along the Pb-I bond, unlike the axes of the bulk $MAPbI_3$. (b) Absorption spectrum of the same nanocrystal for x-, y-, and z-polarized light.

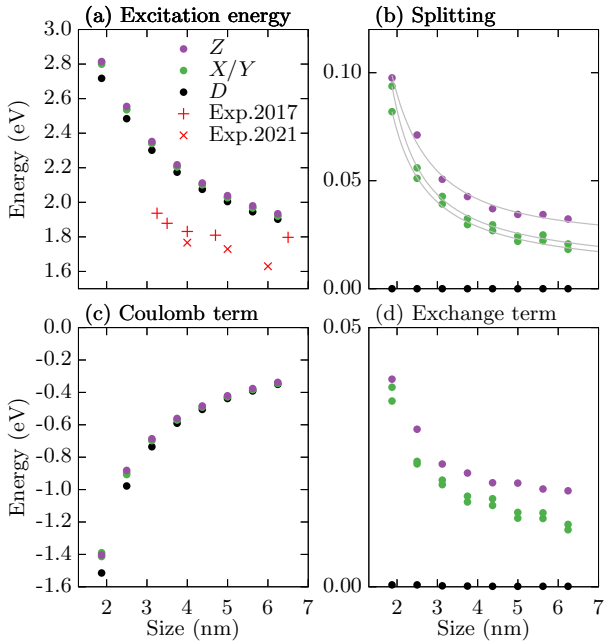

Figure 4: (a) Energy of the first four excited states as a function of the diameter of the nanocrystal. Experimentally measured photoluminescence values are from Refs. 54 (Exp. 2017) and 55 (Exp. 2021). (b) Splitting energy of the first four excitation states with respect to the lowest dark state. Grey lines show the fitting curve for each excitation state. (c) Coulomb term and (d) exchange term contributing to the energy of the first four excited states.

that the polarization axes are aligned parallel to the NC faces, and not along the axes of the tetragonal unit cell shown in Fig. 1(a).

Our BSE calculations enable direct access to atomistic details of the band-edge exciton wavefunctions beyond this simplified picture. As an example, in Fig. 3, we consider a NC with $n = 7$ ($L = 4.4$ nm). In Fig. 3(a), we plot the wavefunctions of the lowest four excitons,

$$\Psi^N(\boldsymbol{r}_e;\bar{\boldsymbol{r}}_h) = \sum_{cv} A^N_{cv}\phi_c(\boldsymbol{r}_e)\phi^*_v(\bar{\boldsymbol{r}}_h) \tag{8}$$

where $\phi_{c/v}(\boldsymbol{r})$ are molecular orbitals, A^N_{cv} is the BSE eigenvector, and we fix the position of the hole $\bar{\boldsymbol{r}}_h$ to the center of the NC. In Fig. 3(b), we show the absorption spectrum with the energy of each transition labeled. Clearly, the lowest energy state is the dark state $|D\rangle$ and the higher energy states are the three bright states $|X\rangle, |Y\rangle, |Z\rangle$, which are labeled according to their polarized absorption spectra. We find the X/Y energy degeneracy to be slightly broken along with a weak violation of the polarization selected rules, which we attribute to the randomly oriented MA cations that lower the crystal symmetry. For this relatively small NC, we see a bright-dark splitting of about 30 meV and an intertriplet splitting of about 3–10 meV.

Extending this analysis to NCs of other sizes, we find that the energy ordering is unchanged and that the lowest energy exciton is a dark state, at least up to $L = 6.2$ nm, as shown in Fig. 4(a). In Fig. 4(b), we plot the bright-dark splitting of the three bright states as a function of the size of the NC. We fit the splitting data to the form $E_s(L) = E_s^\infty + c_1/L + c_2/L^2 + c_3/L^3$, consistent with the binding energy expression in the strong confinement regime.[16] Fitting to our data, we find a nonzero bright-dark splitting of $E_s^\infty = 4$ meV (for X/Y) and 22 meV (for Z) in the $L \to \infty$ limit. The large and positive splitting between Z and D reflects a relatively weak Rashba effect that is insufficient to invert the ordering.[16] We conclude that, within the approximations made here, our simulations predict that the lowest exciton is dark for any sized NC.

Within the GW/BSE approximation, the exciton energies are determined by three factors: the DFT/GW band energies (which reflect the local lattice structure, the carrier confinement, and the dielectric contrast), the electron-hole Coulomb energy (roughly the exciton binding energy), and the electron-hole exchange energy. The latter two quantities are plotted as function of L in Figs. 4(c),(d). As expected, we see that the dark exciton has a vanishing exchange energy and the bright excitons have exchange energies between 40 meV (for small NCs) and 10 meV (for larger NCs). The exciton binding energies due to the screened Coulomb interaction are large and vary from 1.5 eV to 0.3 eV over the same size range. Interestingly, the dark exciton has a slightly larger Coulomb interaction than the bright excitons, a feature which further increases the bright-dark splitting. In fact, for the NC sizes considered here, we find that the differences in the Coulomb term contribute to the bright-dark splitting to the same order of magnitude as the exchange energy.

Finally, we note that the affordable approach taken here allows us to study NCs that are large enough to be compared directly to experimental results on $MAPbI_3$ NCs with $L > 3$ nm, which are indicated in Fig. 4(a). Experimental values come from photoluminescence data of NCs synthesized in the pores of a patterned SiO_2 film.[54,55] We see that our results overestimate the experimental transition energies by about 0.2 eV. This level of accuracy is typical even for fully ab initio GW/BSE calculations and is thus acceptable here, given the additional approximations that were made. Some fraction of this discrepancy may also be attributable to a Stokes shift between absorption and photoluminescence or other exciton-phonon

interactions.

Conclusions

To summarize, we have performed atomistic GW/BSE calculations of the electronic and optical properties of realistically sized $MAPbI_3$ nanocrystals, using parameters determined from ab initio calculations. Within the approximations of our approach, we find large exciton binding energies of over 0.3 eV and that the exciton fine structure is consistent with a spectroscopically dark lowest-lying exciton. The reasonable agreement between our predicted excitation energies and experimentally measured photoluminescence energies supports our methods and findings.

Two approximations in our work are significant and should be revisited for future improvements. The first is the treatment of the atomic structure: geometry relaxation may yield a crystal structure that is different from the bulk tetragonal structure used here. Moreover, the atomic details of the NC surface, including its passivation and reconstruction, might qualitatively change our results, especially for small NCs. The second related approximation is the neglect of electron-phonon coupling. Bulk LHPs are relatively soft and anharmonic materials[73] and strong electron-phonon interactions have been implicated in their electronic properties.[74–76] Recent calculations[65,77] have suggested the importance of lattice screening in determining the exciton properties of LHPs. For example, the authors of Ref. 65 find that the typical BSE exciton binding energy of $CsPbX_3$ is overestimated with respect to experiment by about a factor of three, and that incorporation of phonon screening partially improves the agreement. Given the already high cost of ab initio GW/BSE calculations, we believe that the approximate approach presented here can serve as a basis for future studies of atomic structure, surface reconstruction, electron-phonon coupling, temperature-dependent optical properties, and external dopants.

Associated Content

Supporting Information

The Supporting Information is available free of charge at [publisher inserts link].

Author Information

[publisher inserts author information]

Author Contributions

‖These authors contributed equally to this manuscript.

Present Addresses

Giulia Biffi – Consejo Superior de Investigaciones Científicas, Centro de Física de Materiales, San Sebastián, 20018 Spain
Yeongsu Cho – Department of Chemical Engineering, Massachusetts Institute of Technology, Cambridge, MA 02139 USA

Notes

The authors declare no competing financial interest.

Acknowledgements

This work has been supported by the H2020-MSCA RISE project COMPASS 691185 (G.B.) and by the US Air Force Office of Scientific Research under AFOSR Award No. FA9550-19-1-0405 (Y.C.). The authors acknowledge computing resources from the CINECA Calls award under the ISCRA initiative and from Columbia University's Shared Research Computing Facility project, which is supported by NIH Research Facility Improvement Grant 1G20RR030893-01, and associated funds from the New York State Empire State Development, Division of Science Technology and Innovation (NYSTAR) Contract C090171, both awarded April 15, 2010. The Flatiron Institute is a division of the Simons Foundation.

References

(1) Kovalenko, M. V.; Protesescu, L.; Bodnarchuk, M. I. Properties and potential optoelectronic applications of lead halide perovskite nanocrystals. *Science* **2017**, *358*, 745–750.

(2) Shamsi, J.; Urban, A. S.; Imran, M.; De Trizio, L.; Manna, L. Metal Halide Perovskite Nanocrystals: Synthesis, Post-Synthesis Modifications, and Their Optical Properties. *Chem. Rev.* **2019**, *119*, 3296–3348.

(3) Dey, A.; Ye, J.; De, A.; Debroye, E.; Ha, S. K.; Bladt, E.; Kshirsagar, A. S.; Wang, Z.; Yin, J.; Wang, Y. et al. State of the Art and Prospects for Halide Perovskite Nanocrystals. *ACS Nano* **2021**, *15*, 10775–10981.

(4) Tan, Z. K.; Moghaddam, R. S.; Lai, M. L.; Docampo, P.; Higler, R.; Deschler, F.; Price, M.; Sadhanala, A.; Pazos, L. M.; Credgington, D. et al. Bright light-emitting diodes based on organometal halide perovskite. *Nat. Nanotechnol.* **2014**, *9*, 687–692.

(5) Huang, H.; Polavarapu, L.; Sichert, J. A.; Susha, A. S.; Urban, A. S.; Rogach, A. L. Colloidal lead halide perovskite nanocrystals: synthesis, optical properties and applications. *NPG Asia Mater.* **2016**, *8*, e328–e328.

(6) Lee, S.; Park, J. H.; Nam, Y. S.; Lee, B. R.; Zhao, B.; Di Nuzzo, D.; Jung, E. D.; Jeon, H.; Kim, J. Y.; Jeong, H. Y. et al. Growth of Nanosized Single Crystals for Efficient Perovskite Light-Emitting Diodes. *ACS Nano* **2018**, *12*, 3417–3423.

(7) Palei, M.; Caligiuri, V.; Kudera, S.; Krahne, R. Robust and Bright Photoluminescence from Colloidal Nanocrystal/Al2O3 Composite Films Fabricated by Atomic Layer Deposition. *ACS Appl. Mater. Interfaces* **2018**, *10*, 22356–22362.

(8) Akkerman, Q. A.; Rainò, G.; Kovalenko, M. V.; Manna, L. Genesis, challenges and opportunities for colloidal lead halide perovskite nanocrystals. *Nat. Mater.* **2018**, *17*, 394–405.

(9) Sutherland, B. R.; Sargent, E. H. Perovskite photonic sources. *Nat. Photonics* **2016**, *10*, 295–302.

(10) Caligiuri, V.; Palei, M.; Imran, M.; Manna, L.; Krahne, R. Planar Double-Epsilon-Near-Zero Cavities for Spontaneous Emission and Purcell Effect Enhancement. *ACS Photonics* **2018**, *5*, 2287–2294.

(11) Shrivastava, M.; Bodnarchuk, M. I.; Hazarika, A.; Luther, J. M.; Beard, M. C.; Kovalenko, M. V.; Adarsh, K. V. Polaron and Spin Dynamics in Organic–Inorganic Lead Halide Perovskite Nanocrystals. *Adv. Opt. Mater.* **2020**, *8*, 2001016.

(12) Imran, M.; Caligiuri, V.; Wang, M.; Goldoni, L.; Prato, M.; Krahne, R.; Trizio, L. D.; Manna, L. Benzoyl Halides as Alternative Precursors for the Colloidal Synthesis of Lead-Based Halide Perovskite Nanocrystals. *J. Am. Chem. Soc* **2018**, *140*, 37.

(13) Fu, M.; Tamarat, P.; Huang, H.; Even, J.; Rogach, A. L.; Lounis, B. Neutral and Charged Exciton Fine Structure in Single Lead Halide Perovskite Nanocrystals Revealed by Magneto-optical Spectroscopy. *Nano Lett.* **2017**, *17*, 2895–2901.

(14) Becker, M. A.; Vaxenburg, R.; Nedelcu, G.; Sercel, P. C.; Shabaev, A.; Mehl, M. J.; Michopoulos, J. G.; Lambrakos, S. G.; Bernstein, N.; Lyons, J. L. et al. Bright triplet excitons in caesium lead halide perovskites. *Nature* **2018**, *553*, 189–193.

(15) Sercel, P. C.; Lyons, J. L.; Bernstein, N.; Efros, A. L. Quasicubic model for metal halide perovskite nanocrystals. *J. Chem. Phys.* **2019**, *151*, 234106.

(16) Sercel, P. C.; Lyons, J. L.; Wickramaratne, D.; Vaxenburg, R.; Bernstein, N.; Efros, A. L. Exciton Fine Structure in Perovskite Nanocrystals. *Nano Lett.* **2019**, *19*, 4068–4077.

(17) Tamarat, P.; Bodnarchuk, M. I.; Trebbia, J. B.; Erni, R.; Kovalenko, M. V.; Even, J.; Lounis, B. The ground exciton state of formamidinium lead bromide perovskite nanocrystals is a singlet dark state. *Nat. Mater.* **2019**, *18*, 717–724.

(18) Rossi, D.; Liu, X.; Lee, Y.; Khurana, M.; Puthenpurayil, J.; Kim, K.; Akimov, A. V.; Cheon, J.; Son, D. H. Intense Dark Exciton Emission from Strongly Quantum-Confined CsPbBr 3 Nanocrystals. *Nano Lett.* **2020**,

(19) Rossi, D.; Qiao, T.; Liu, X.; Khurana, M.; Akimov, A. V.; Cheon, J.; Son, D. H. Size-dependent dark exciton properties in cesium lead halide perovskite quantum dots. *J. Chem. Phys.* **2020**, *153*, 184703.

(20) Ben Aich, R.; Saïdi, I.; Ben Radhia, S.; Boujdaria, K.; Barisien, T.; Legrand, L.; Bernardot, F.; Chamarro, M.; Testelin, C. Bright-Exciton Splittings in Inorganic Cesium Lead Halide Perovskite Nanocrystals. *Phys. Rev. Appl.* **2019**, *11*, 034042.

(21) Katan, C.; Mercier, N.; Even, J. Quantum and Dielectric Confinement Effects in Lower-Dimensional Hybrid Perovskite Semiconductors. *Chem. Rev.* **2019**, *119*, 3140–3192.

(22) Amat, A.; Mosconi, E.; Ronca, E.; Quarti, C.; Umari, P.; Nazeeruddin, M. K.; Grätzel, M.; De Angelis, F. Cation-induced band-gap tuning in organohalide perovskites: Interplay of spin-orbit coupling and octahedra tilting. *Nano Lett.* **2014**, *14*, 3608–3616.

(23) Motta, C.; El-Mellouhi, F.; Kais, S.; Tabet, N.; Alharbi, F.; Sanvito, S. Revealing the role of organic cations in hybrid halide perovskite CH3 NH3PbI3. *Nat. Commun.* **2015**, *6*, 1–7.

(24) Mehdizadeh, A.; Akhtarianfar, S. F.; Shojaei, S. Role of Methylammonium Rotation in Hybrid Halide MAPbX3 (X = I, Br, and Cl) Perovskites by a Density Functional Theory Approach: Optical and Electronic Properties. *J. Phys. Chem. C* **2019**, *123*, 6725–6734.

(25) Saleh, G.; Biffi, G.; Di Stasio, F.; Martín-Garciá, B.; Abdelhady, A. L.; Manna, L.; Krahne, R.; Artyukhin, S. Methylammonium Governs Structural and Optical Properties of Hybrid Lead Halide Perovskites through Dynamic Hydrogen Bonding. *Chem. Mater.* **2021**, *33*, 8524–8533.

(26) Blundell, S. A.; Guet, C. All-order correlation of single excitons in nanocrystals using a $k \cdot p$ envelope-function approach: Application to lead halide perovskites. *Phys. Rev. B* **2022**, *105*, 155420.

(27) Buin, A.; Comin, R.; Ip, A. H.; Sargent, E. H. Perovskite Quantum Dots Modeled Using ab Initio and Replica Exchange Molecular Dynamics.

(28) Ten Brinck, S.; Infante, I. Surface Termination, Morphology, and Bright Photoluminescence of Cesium Lead Halide Perovskite Nanocrystals. *ACS Energy Lett.* **2016**, *1*, 1266–1272.

(29) Ten Brinck, S.; Zaccaria, F.; Infante, I. Defects in lead halide perovskite nanocrystals: Analogies and (many) differences with the bulk. *ACS Energy Lett.* **2019**, *4*, 2739–2747.

(30) Perez, C. M.; Ghosh, D.; Prezhdo, O.; Tretiak, S.; Neukirch, A. J. Excited-State Properties of Defected Halide Perovskite Quantum Dots: Insights from Computation. *J. Phys. Chem. Lett.* **2021**, *12*, 1005–1011.

(31) Hedin, L. New Method for Calculating the One-Particle Green's Function with Application to the Electron-Gas Problem. *Phys. Rev.* **1965**, *139*, A796–A823.

(32) Strinati, G.; Mattausch, H. J.; Hanke, W. Dynamical Correlation Effects on the Quasiparticle Bloch States of a Covalent Crystal. *Phys. Rev. Lett.* **1980**, *45*, 290–294.

(33) Hybertsen, M. S.; Louie, S. G. Electron correlation in semiconductors and insulators: Band gaps and quasiparticle energies. *Phys. Rev. B* **1986**, *34*, 5390–5413.

(34) Albrecht, S.; Reining, L.; Sole, R. D.; Onida, G. Ab Initio Calculation of Excitonic Effects in the Optical Spectra of Semiconductors. *Phys. Rev. Lett.* **1998**, *80*, 4510–4513.

(35) Benedict, L. X.; Shirley, E. L.; Bohn, R. B. Optical Absorption of Insulators and the Electron-Hole Interaction: An Ab Initio Dynamical Correlation Effects on the Quasiparticle Bloch States of a Covalent Crystal. *Phys. Rev. Lett.* **1998**, *80*, 4514–4517.

(36) Rohlfing, M.; Louie, S. G. Electron-Hole Excitations in Semiconductors and Insulators. *Phys. Rev. Lett.* **1998**, *81*, 2312–2315.

(37) Cho, Y.; Berkelbach, T. C. Optical Properties of Layered Hybrid Organic-Inorganic Halide Perovskites: A Tight-Binding GW-BSE Study. *J. Phys. Chem. Lett.* **2019**, *10*, 6189–6196.

(38) Kojima, A.; Teshima, K.; Shirai, Y.; Miyasaka, T. Organometal halide perovskites as visible-light sensitizers for photovoltaic cells. *J. Am. Chem. Soc.* **2009**, *131*, 6050–6051.

(39) Im, J. H.; Lee, C. R.; Lee, J. W.; Park, S. W.; Park, N. G. 6.5% efficient perovskite quantum-dot-sensitized solar cell. *Nanoscale* **2011**, *3*, 4088–4093.

(40) Cadelano, M.; Sarritzu, V.; Sestu, N.; Marongiu, D.; Chen, F.; Piras, R.; Corpino, R.; Carbonaro, C. M.; Quochi, F.; Saba, M. et al. Can Trihalide Lead Perovskites Support Continuous Wave Lasing? *Adv. Opt. Mater.* **2015**, *3*, 1557–1564.

(41) Xiao, Z.; Yan, Y. Progress in Theoretical Study of Metal Halide Perovskite Solar Cell Materials. *Adv. Energy Mater.* **2017**, *7*, 1701136.

(42) Filippetti, A.; Delugas, P.; Saba, M. I.; Mattoni, A. Entropy-Suppressed Ferroelectricity in Hybrid Lead-Iodide Perovskites. *J. Phys. Chem. Lett.* **2015**, *6*, 4909–4915.

(43) Frohna, K.; Deshpande, T.; Harter, J.; Peng, W.; Barker, B. A.; Neaton, J. B.; Louie, S. G.; Bakr, O. M.; Hsieh, D.; Bernardi, M. Inversion symmetry and bulk Rashba effect in methylammonium lead iodide perovskite single crystals. *Nat. Commun.* **2018**, *9*, 1–9.

(44) Umari, P.; Mosconi, E.; De Angelis, F. Relativistic GW calculations on CH3NH3PbI3 and CH3NH3SnI3 Perovskites for Solar Cell Applications. *Sci. Rep.* **2014**, *4*, 1–7.

(45) Brivio, F.; Butler, K. T.; Walsh, A.; van Schilfgaarde, M. Relativistic quasiparticle self-consistent electronic structure of hybrid halide perovskite photovoltaic absorbers. *Phys. Rev. B* **2014**, *89*, 155204.

(46) Filip, M. R.; Giustino, F. GW quasiparticle band gap of the hybrid organic-inorganic perovskite CH3NH3PbI3: Effect of spin-orbit interaction, semicore electrons, and self-consistency. *Phys. Rev. B* **2014**, *90*, 245145.

(47) Filip, M. R.; Verdi, C.; Giustino, F. GW Band Structures and Carrier Effective Masses of CH3NH3PbI3 and Hypothetical Perovskites of the Type APbI3: A=NH4, PH4, AsH4, and SbH4. *J. Phys. Chem. C* **2015**, *119*, 25209–25219.

(48) Schmidt, L. C.; Pertegás, A.; González-Carrero, S.; Malinkiewicz, O.; Agouram, S.; Espallargas, G. M.; Bolink, H. J.; Galian, R. E.; Pérez-Prieto, J. Nontemplate Synthesis of CH3NH3PbBr3 Perovskite Nanoparticles. *J. Am. Chem. Soc.* **2014**, *136*, 850–853.

(49) Zhang, F.; Zhong, H.; Chen, C.; gang Wu, X.; Hu, X.; Huang, H.; Han, J.; Zou, B.; Dong, Y. Brightly Luminescent and Color-Tunable Colloidal CH3NH3PbX3 (X = Br, I, Cl) Quantum Dots: Potential Alternatives for Display Technology. *ACS Nano* **2015**, *9*, 4533–4542.

(50) Huang, H.; Susha, A. S.; Kershaw, S. V.; Hung, T. F.; Rogach, A. L. Control of Emission Color of High Quantum Yield CH3NH3PbBr3 Perovskite Quantum Dots by Precipitation Temperature. *Advanced Science* **2015**, *2*, 1500194.

(51) Xiao, Z.; Kerner, R. A.; Tran, N.; Zhao, L.; Scholes, G. D.; Rand, B. P. Engineering Perovskite Nanocrystal Surface Termination for Light-Emitting Diodes with External Quantum Efficiency Exceeding 15%. *Adv. Funct. Mater.* **2019**, *29*, 1807284.

(52) Zhang, B.; Goldoni, L.; Lambruschini, C.; Moni, L.; Imran, M.; Pianetti, A.; Pinchetti, V.; Brovelli, S.; De Trizio, L.; Manna, L. Stable and Size Tunable CsPbBr3Nanocrystals Synthesized with Oleylphosphonic Acid. *Nano Lett.* **2020**, *20*, 8847–8853.

(53) Ijaz, P.; Imran, M.; Soares, M. M.; Tolentino, H. C.; Martín-García, B.; Giannini, C.; Moreels, I.; Manna, L.; Krahne, R. Composition-, Size-, and Surface Functionalization-Dependent Optical Properties of Lead Bromide Perovskite Nanocrystals. *J. Phys. Chem. Lett.* **2020**, *11*, 2079–2085.

(54) Anaya, M.; Rubino, A.; Rojas, T. C.; Galisteo-López, J. F.; Calvo, M. E.; Míguez, H. Strong Quantum Confinement and Fast Photoemission Activation in CH3NH3PbI3 Perovskite Nanocrystals Grown within Periodically Mesostructured Films. *Adv. Opt. Mater.* **2017**, *5*, 1601087.

(55) Rubino, A.; Francisco-López, A.; Barker, A. J.; Petrozza, A.; Calvo, M. E.; Goñi, A. R.; Míguez, H. Disentangling Electron-Phonon Coupling and Thermal Expansion Effects in the Band Gap Renormalization of Perovskite Nanocrystals. *J. Phys. Chem. Lett.* **2021**, *12*, 569–575.

(56) Whitfield, P.; Herron, N.; Guise, W.; Page, K.; Cheng, Y.; Milas, I.; Crawford, M. Structures, Phase Transitions and Tricritical Behavior of the Hybrid Perovskite Methyl Ammonium Lead Iodide. *Sci. Rep.* **2016**, *6*, 35685.

(57) Giannozzi, P.; Baroni, S.; Bonini, N.; Calandra, M.; Car, R.; Cavazzoni, C.; Ceresoli, D.; Chiarotti, G. L.; Cococcioni, M.; Dabo, I. et al. QUANTUM ESPRESSO: a modular and open-source software project for quantum simulations of materials. *J. Phys.: Condens. Matter* **2009**, *21*, 395502.

(58) Perdew, J. P.; Burke, K.; Ernzerhof, M. Generalized Gradient Approximation Made Simple. *Phys. Rev. Lett.* **1996**, *77*, 3865–3868.

(59) Mostofi, A. A.; Yates, J. R.; Lee, Y. S.; Souza, I.; Vanderbilt, D.; Marzari, N. wannier90: A tool for obtaining maximally-localised Wannier functions. *Comput. Phys. Commun.* **2008**, *178*, 685–699.

(60) Brus, L. E. A simple model for the ionization potential, electron affinity, and aqueous redox potentials of small semiconductor crystallites. *J. Chem. Phys.* **1983**, *79*, 5566–5571.

(61) Brus, L. E. Electron-electron and electron-hole interactions in small semiconductor crystallites: The size dependence of the lowest excited electronic state. *J. Chem. Phys.* **1984**, *80*, 4403–4409.

(62) Neaton, J. B.; Hybertsen, M. S.; Louie, S. G. Renormalization of Molecular Electronic Levels at Metal-Molecule Interfaces. *Phys. Rev. Lett.* **2006**, *97*, 216405.

(63) Yang, P.-K.; Liaw, S.-H.; Lim, C. Representing an Infinite Solvent System with a Rectangular Finite System Using Image Charges. *J. Phys. Chem. B* **2002**, *106*, 2973.

(64) Dirin, D. N.; Protesescu, L.; Trummer, D.; Kochetygov, I. V.; Yakunin, S.; Krumeich, F.; Stadie, N. P.; Kovalenko, M. V. Harnessing Defect-Tolerance at the Nanoscale: Highly Luminescent Lead Halide Perovskite Nanocrystals in Mesoporous Silica Matrixes. *Nano Lett.* **2016**, *16*, 5866–5874.

(65) Filip, M. R.; Haber, J. B.; Neaton, J. B. Phonon Screening of Excitons in Semiconductors: Halide Perovskites and Beyond. *Phys. Rev. Lett.* **2021**, *127*, 067401.

(66) Sun, Q.; Berkelbach, T. C.; Blunt, N. S.; Booth, G. H.; Guo, S.; Li, Z.; Liu, J.; McClain, J. D.; Sayfutyarova, E. R.; Sharma, S. et al. PySCF: the Python-based simulations of chemistry framework. *WIREs Comput. Mol. Sci.* **2017**, *8*.

(67) Sun, Q.; Zhang, X.; Banerjee, S.; Bao, P.; Barbry, M.; Blunt, N. S.; Bogdanov, N. A.; Booth, G. H.; Chen, J.; Cui, Z.-H. et al. Recent developments in the PySCF program package. *J. Chem. Phys.* **2020**, *153*, 024109.

(68) Weigend, F.; Ahlrichs, R. Balanced basis sets of split valence, triple zeta valence and quadruple zeta valence quality for H to Rn: Design and assessment of accuracy. *Phys. Chem. Chem. Phys.* **2005**, *7*, 3297.

(69) Miyata, A.; Mitioglu, A.; Plochocka, P.; Portugall, O.; Wang, J. T.-W.; Stranks, S. D.; Snaith, H. J.; Nicholas, R. J. Direct measurement of the exciton binding energy and effective masses for charge carriers in organic–inorganic tri-halide perovskites. *Nat. Phys.* **2015**, *11*, 582–587.

(70) Galkowski, K.; Mitioglu, A.; Miyata, A.; Plochocka, P.; Portugall, O.; Eperon, G. E.; Wang, J. T.-W.; Stergiopoulos, T.; Stranks, S. D.; Snaith, H. J. et al. Determination of the exciton binding energy and effective masses for methylammonium and formamidinium lead tri-halide perovskite semiconductors. *Energ. Environ. Sci.* **2016**, *9*, 962–970.

(71) Yang, Z.; Surrente, A.; Galkowski, K.; Bruyant, N.; Maude, D. K.; Haghighirad, A. A.; Snaith, H. J.; Plochocka, P.; Nicholas, R. J. Unraveling the Exciton Binding Energy and the Dielectric Constant in Single-Crystal Methylammonium Lead Triiodide Perovskite. *J. Phys. Chem. Lett.* **2017**, *8*, 1851–1855.

(72) Even, J. Pedestrian Guide to Symmetry Properties of the Reference Cubic Structure of 3D All-Inorganic and Hybrid Perovskites. *J. Phys. Chem. Lett.* **2015**, *6*, 2238–2242.

(73) Yaffe, O.; Guo, Y.; Tan, L. Z.; Egger, D. A.; Hull, T.; Stoumpos, C. C.; Zheng, F.; Heinz, T. F.; Kronik, L.; Kanatzidis, M. G. et al. Local Polar Fluctuations in Lead Halide Perovskite Crystals. *Phys. Rev. Lett.* **2017**, *118*, 136001.

(74) Wright, A. D.; Verdi, C.; Milot, R. L.; Eperon, G. E.; Pérez-Osorio, M. A.; Snaith, H. J.; Giustino, F.; Johnston, M. B.; Herz, L. M. Electron–phonon coupling in hybrid lead halide perovskites. *Nat. Commun.* **2016**, *7*.

(75) Saidi, W. A.; Kachmar, A. Effects of Electron–Phonon Coupling on Electronic Properties of Methylammonium Lead Iodide Perovskites. *J. Phys. Chem. Lett.* **2018**, *9*, 7090–7097.

(76) Mayers, M. Z.; Tan, L. Z.; Egger, D. A.; Rappe, A. M.; Reichman, D. R. How Lattice and Charge Fluctuations Control Carrier Dynamics in Halide Perovskites. *Nano Lett.* **2018**, *18*, 8041–8046.

(77) Park, Y.; Obliger, A.; Limmer, D. T. Nonlocal Screening Dictates the Radiative Lifetimes of Excitations in Lead Halide Perovskites. *Nano Lett.* **2022**, *22*, 2398–2404.